

Ultrasonic-assisted solvothermal synthesis of self-assembled Copper Ferrite nanoparticles

Ahmad Reza Abbasian^{1,*}, Samira Sadat Hosseini², Masoud Shayesteh², Mahdi Shafiee Afarani¹,
Masoud Rafigh Esmailzaei³

¹ Department of Materials Engineering, Faculty of Engineering, University of Sistan and Baluchestan, Zahedan, Iran

² Department of Chemical Engineering, Faculty of Engineering, University of Sistan and Baluchestan, Zahedan, Iran

³ Department of Chemistry, Faculty of Sciences, University of Sistan and Baluchestan, Zahedan, Iran

Received 04 December 2019; revised 15 February 2020; accepted 28 February 2020; available online 17 March 2020

Abstract

The aim of this work was to characterize copper ferrite nanoparticles synthesized via solvothermal method and to investigate the effects of ultrasonic waves on the synthesis efficiency. Crystal structure, functional groups, microstructure, particle size, magnetic properties, specific surface area, porosity distribution and photocatalytic activity of the synthesized nanoparticles were also investigated. Structural analyses revealed that nanostructured copper ferrites with spinel crystal structure have been successfully synthesized via both solvothermal and ultrasonic-assisted solvothermal methods. The powders contained submicron spheres which were consisted of nanoparticles with regular arrangement. The applied ultrasonic wave had significant effect on the shape and size of the spheres, particularly on their specific surface area, but it had no considerable effect on the magnetic properties. All the synthesized powders were superparamagnetic and their band gap energy was about 1.5 eV. High absorption rate is another unique characteristic of the powders so that it can complete the photocatalytic process in less than 10 min. The saturation magnetization of about 47 emu/g, together with negligible coercivity, make the synthesized nanostructured absorbent ideal for magnetic separation processes.

Keywords: Copper Ferrite; Methyl Orange; Photocatalyst; Solvothermal; Superparamagnetic; Ultrasonic Waves.

How to cite this article

Abbasian AR, Sadat Hosseini S, Shayesteh M, Shafiee Afarani M, Rafigh Esmailzaei M. Ultrasonic-assisted solvothermal synthesis of self-assembled Copper Ferrite nanoparticles. *Int. J. Nano Dimens.*, 2020; 11 (2): 130-144.

INTRODUCTION

Nowadays, more toxic wastewaters are produced by textile, paper, plastic and dyeing industries, mostly consisted of pollutants which contain azo dyes [1-3]. Their toxic nature and harmful effects on the health of living organisms are the main reasons for their removal from wastewaters [4]. One of the most well-known solutions for degradation of azo dyes is photocatalytic process [5]. Various nanomaterials have been subjected to the photocatalytic degradation [6, 7]. Nano-titania (TiO₂) is a common photocatalyst [8-10] which is now commercially available [11]. However, it is only activated under UV radiation due to its

band gap [8]. To overcome this limitation, one solution is to exploit photocatalysts with small band gaps [12]. These materials have promising activity and performance under visible light. Low energy consumption and elimination of harmful effects of UV radiation are the main advantages of using these photocatalysts [13]. On the other hand, separation of the photocatalyst from the medium after dye degradation is one of the most important challenges. Therefore, immobilizing the nanoparticles or coatings on macro-scale support beads or granules is a subject of recent research studies [14]. Also, magnetization of the photocatalyst has been proposed to separate the photocatalyst from the medium by applying

* Corresponding Author Email: abbasian@eng.usb.ac.ir

a magnetic field [15]. Core-shell materials are good example of such photocatalysts [15]. A new approach has been proposed in which magnetic photocatalysts such as ferrites [16, 17] are applied. These photocatalysts have excellent magnetic properties together with good recovering ability for prolonged usage.

Among various ferrite materials, copper ferrite nanoparticles are good candidates because of their small band gap and desirable magnetic properties [16, 18]. Particles should be superparamagnetic in order to have a uniform dispersion and prevent them from agglomeration. So, the particle size should be less than a critical nanometer value. However, for nanoparticles, as the particle size decreases, its amenability to an external magnetic field decreases, which will not be large sufficient to prevail the Brownian motion. Therefore, no efficient magnetic separation will happen [19]. To overcome this problem, sub-micrometer hierarchical structures that form from nanoparticles are proposed as useful strategy [19]. Each constituent unit in hierarchical nanostructures is under a critical size which resulted in superparamagnetic properties [20-22]. Furthermore, they exhibit high specific surface area because of the numerous interparticle spaces or intraparticle pores [23, 24]. In addition, hierarchical nanostructures exhibit satisfactory magnetic performance due to their larger size and weaker Brownian motion [19].

CuFe_2O_4 nanomaterial is synthesized by various methods including solid-state reaction [25], combustion synthesis [26], sol-gel strategy [27], co-precipitation [28], hydrothermal [29] and solvothermal [30] methods, etc. Nevertheless, one of the best methods for the synthesis of hierarchical nanostructures is self-assembly of nanoparticles via solvothermal method [21]. This method is an easy and economical way to control the synthesis process and the self-assembly of the nanoparticles [31].

Ferrite nanoparticles with diverse properties have been obtained depending on the used raw materials and the reaction conditions. Several studies have reported the synthesis of hierarchical copper ferrite powders via solvothermal method [23, 24, 30, 32-40]. The synthesis of copper ferrite via solvothermal method is usually carried out by the reduction of iron and copper chlorides/nitrates with ethylene glycol (EG). In the synthetic systems, sodium acetate is used as electrostatic stabilizer.

Hierarchical CuFe_2O_4 nanostructures synthesized by solvothermal method have attracted a lot of interest owing to their potential applications in magnetic resonance imaging (MRI) [39], gas sensor [30], determination of dyes [35], infrared radiation materials [33], supercapacitors [23], selective capturing of proteins [38] and photo catalysis [40]. For these applications, the morphology of the particles plays a vital role. Shen *et al.* [40] studied the visible-light-induced photocatalytic conversion of benzene over CuFe_2O_4 nanospheres. They obtained spherical nanomaterials with excellent ability to remove organic pollutants in the atmosphere.

Some researchers have applied ultrasonic assisted solvothermal routes for the synthesis of powders [41]. However, to the best of our knowledge, the combination of ultrasonication and solvothermal methods for the synthesis of CuFe_2O_4 powder has not reported yet. The aim of the present study was the synthesis of self-assembled copper ferrite nanoparticles with spherical structure via solvothermal method, ultrasonic method, and ultrasonic-assisted solvothermal method. Also, photocatalytic activity of the hierarchical CuFe_2O_4 was evaluated via the photocatalytic conversion of methyl orange under different irradiation conditions. Several characteristics of the obtained nanopowders including molecular structure, microstructure, specific surface area, photocatalytic activity and magnetic properties were investigated.

MATERIALS AND METHODS

Raw materials

Raw materials used in this work are listed in Table 1. All the reagents were purchased from Merck (Germany) and used as received without further purification.

Synthesis procedure

In this study, three different methods are used for the synthesis of copper ferrite, namely ultrasonic method (U), solvothermal method (ST) and ultrasonic-assisted solvothermal method (UAS).

Ultrasonic method

Probe ultrasonic device with the working frequency of 20 kHz and power of 400 W (Ultrasonic Technology Development Co., Iran) was used for ultrasonic synthesis method. The

Table 1. Specification of raw materials.

Compound name	Chemical formula	Molar mass (g/mol)	Product code
Copper(II) chloride dihydrate	CuCl ₂ ·2H ₂ O	170.48	10733
Iron (III) chloride hexahydrate	FeCl ₃ ·6H ₂ O	270.33	103943
Sodium acetate anhydrous	CH ₃ COONa	82.03	106268
Ethylene glycol	C ₂ H ₆ O ₂	62.07	109621
Methyl orange	C ₁₄ H ₁₄ N ₃ NaO ₃ S	327.34	101322

synthesis solution was prepared by solving 0.811 g FeCl₃·6H₂O in 29.4 mL ethylene glycol. Then, 0.256 g CuCl₂·2H₂O and 1.23 g sodium acetate were added to the solution and stirred at 700 rpm for 10 min using magnetic stirrer. The obtained solution was exposed to ultrasonic waves with the power of 350 W for 30 and 60 min. It is worth noting that initial solution was green while the color of the solution became darker during the ultrasonic process. Further ultrasonication for 60 min had no significant effect on the color. The samples were named as U30 and U60, respectively. After each 1min, ultrasonication was stopped for 2 min to cool down the solution. Finally, the sediments were separated by centrifugation at 6000 rpm, washed three times with distilled water and oven-dried at 60 °C for 12 h.

Solvothermal method

The synthesis solution was prepared by solving 0.811 g FeCl₃·6H₂O in 29.4 mL ethylene glycol. Then, 0.256 g CuCl₂·2H₂O and 1.23 g sodium acetate were added to the solution and stirred at 700 rpm for 10 min using magnetic stirrer. Then, the solution was poured into cylindrical stainless steel autoclave (70 mL) with Teflon lining. The autoclave was placed in oven at 200 °C for 12 h. After cooling the autoclave, the sediment was centrifuged, washed three times with distilled water and finally oven-dried at 60 °C for 12 h. The sample prepared via this method was named as ST.

Ultrasonic-assisted solvothermal method

First, the synthesis solution was prepared by solving 0.811 g FeCl₃·6H₂O in 29.4 mL ethylene glycol. Then, 0.256 g CuCl₂·2H₂O and 1.23 g sodium acetate were added to the solution and stirred at 700 rpm for 10 min using magnetic stirrer. The obtained solution was exposed to ultrasonic waves with the power of 350 W for 30 and 60 min. Then, the obtained solution was poured into cylindrical stainless steel autoclave (70 mL) with Teflon lining. The autoclave was placed in oven at 200 °C for 12

h. After cooling the autoclave, the sediments were centrifuged, washed three times with distilled water and finally oven-dried at 60 °C for 12 h. The samples synthesized via this method were named as UAS30 and UAS60.

Characterization

X-ray diffractometer (XRD, Bruker, Advance D8, Germany) with a Cu-K α radiation tube was used for phase analysis. Crystallite size was calculated using Scherrer equation[42]:

$$D = 0.9 \lambda / \beta \cos \theta \quad (1)$$

where D is the crystallite size (nm), λ is the X-ray wavelength (nm), β is the half-height width of the diffraction peak (radian), and θ is the diffraction angle.

Fourier Transform Infrared spectroscopy (FTIR, Bruker Tensor II, Germany) was performed to determine organic compounds and functional groups. Morphology and size of the nanoparticles were evaluated by scanning electron microscope (SEM, KYKY3900, china) and field emission SEM (FESEM, Mira 3-XMU, Czech). Particle size distribution was determined using Image J software by measuring at least 100 particles.

Nitrogen gas adsorption/desorption curves were obtained at 77 K using Belspor-mini II apparatus (Japan), before which, samples were heated in vacuum for at least 2 h. Specific surface area, total pore volume and mean pore size were measured using desorption curves and Brunauer-Emmett-Teller (BET) method while mesopore size distribution was determined using adsorption curves and Barrett, Joyner, and Halenda (BJH) method. Magnetic properties were examined by a vibrating-sample magnetometer (VSM) device model MDK (Meghnatis Daghigh Kavir Co, Kashan, Iran). Dual beam spectrophotometer (UV-JASCO 570, Japan) was used for measuring the adsorption spectra. Band gap energy (E_g) was estimated using adsorption data according to Mills *et al.* [43] procedure and Tauc formula [44].

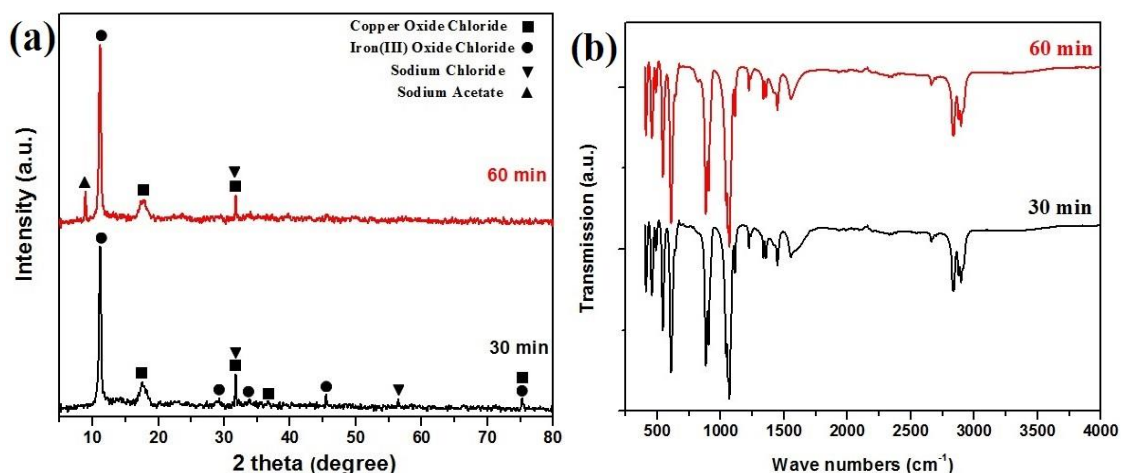


Fig. 1. (a) XRD patterns and (b) FTIR spectra for U30 and U60 samples.

$$(\alpha h\nu)^n = \text{Const} (h\nu - E_g) \quad (2)$$

where α is the adsorption value, h is the Plank's constant and ν is the light frequency. E_g was determined by plotting $(\alpha h\nu)^n$ versus $h\nu$ according to equation 2.

Dye removal

Methyl orange solution in distilled water (15 M or 500 mgL⁻¹) was diluted to obtain solutions with concentrations of 5, 10, 15, 25 and 45 mgL⁻¹, respectively. The maximum adsorption for solutions, measured by UV-Vis spectrophotometer in the wavelength range of 200-800 nm, was observed at 465 nm. The adsorption measurement was repeated for diluted solutions to obtain a calibration curve between methyl orange concentration and adsorption at 465 nm.

In order to evaluate the methyl orange adsorption under three different conditions (i.e. visible light, 254 nm UV light and darkness), 0.02 g of the adsorbent was added to 20 mL of 15 M methyl orange solution. After centrifugation, methyl orange adsorption by the adsorbent after 10-100 min was determined using UV-Vis spectroscopy. For all the solutions, adsorption at 465 nm was considered as a measure for methyl orange concentration. Methyl orange adsorption by nanoparticles was determined and then the adsorption curve was plotted versus time.

The removal efficiency (degradation percentage) and adsorption capacity of the samples for methyl orange dye were calculated using equations (3) and (4), respectively:

$$\text{Degradation (\%)} = \frac{C_0 - C}{C_0} \times 100 \quad (3)$$

$$q = \frac{(C_0 - C)V}{m} \quad (4)$$

where q is the adsorption capacity (mg g⁻¹), C_0 and C are the concentration of methyl orange solution at initial and a specific time (mg L⁻¹), respectively, m is the weight of the CuFe₂O₄ adsorbent (g), and V is the volume of the solution (mL).

RESULTS AND DISCUSSION

Ultrasonic synthesis method

Structural and molecular analyses

XRD patterns for samples prepared using ultrasonic method for 30 and 60min (i.e. U30 and U60) are shown in Fig. 1a. As can be seen, iron and copper oxychlorides have deposited after 30min ultrasonication (JCPDS card no. 96-101-0310 and 00-035-0679, respectively). Some sodium chloride salt (JCPDS card no 00-005-0628) has also formed. Despite washing the sediments several times by distilled water after ultrasonication, some undissolved salts were remained in the sediment. It seems that the salt crystals have acted as nucleating sites for copper and iron oxychlorides which do not dissolve in water. By increasing the ultrasonication time to 60min, peaks related to sodium acetate are also appeared (JCPDS card no 00-029-1158). It can be concluded that at longer ultrasonication times, sodium acetate (similar to sodium chloride) has deposited and acted as

nucleating site for the formation of copper and iron oxychlorides. So, it can be declared that sodium chloride and sodium acetate salts have initially formed via ultrasonic waves and then iron and copper oxychlorides have deposited on them.

FTIR spectra of the U30 and U60 samples are shown in Fig. 1b. Peaks at 2895, 2838, 1446, 1356, 1221, 1111, 1067, 903 and 881 cm^{-1} arise from molecular vibrations in ethylene glycol. The results are in accordance with the FTIR results reported for ethylene glycol in [45]. Peak observed at 541 cm^{-1} is also corresponded to ethylene glycol [46]. Peaks at 607, 488, 455 and 408 cm^{-1} are attributed to metallic bond vibrations in copper and iron oxychlorides [47]. There is no obvious difference between the spectra of these two samples.

Microstructural evaluation

SEM images for U30 and U60 samples are shown in Fig. 2. It can be seen from Fig. 2a that particles in the U30 sample have irregular morphologies. It seems that the particles have irregular shapes because of the turbulence in the reaction medium. Although some particles are agglomerated (Fig.2b), most of them are well-dispersed (Fig.2c). On the other hand, U60 sample also has irregular morphology (Fig. 2d). However, in contrast to U30 sample, the agglomerated particles are dominant (Fig. 2e). It is interesting that dispersed particles in U60 sample (Fig.2f) have the same microstructure as the dispersed particles in the U30 sample.

According to XRD results, sodium chloride is formed in the U30 sample. However, further sodium acetate is formed with increasing the ultrasonication time. In the U30 sample, sodium chloride has acted as nucleating sites, while sodium acetate had the same role in the U60 sample. Iron and copper oxychlorides deposited on the sodium acetate are mainly agglomerated, while they are well-dispersed on the sodium chloride. This may be attributed to the fact that sodium acetate nuclei are continuous, but sodium chloride nuclei are dispersed.

Ultrasonic-assisted solvothermal synthesis method Structural and molecular analyses

XRD patterns for the samples synthesized via ultrasonic-assisted solvothermal method for 0, 30 and 60 min (i.e. ST, UAS30 and UAS60 samples, respectively) are shown in Fig. 3a. It can be seen that the ST sample contains cubic copper ferrite

crystals (JCPDS card no. 0010-077-01), crystalline copper oxide (JCPDS card no. 03-065-3288), crystalline metallic copper (JCPDS card no. 01-070-3038) and sodium chloride (JCPDS card no. 00-088-2300). Ethylene glycol is a strong reducing agent and the reducing potential for converting Cu^{2+} to metallic Cu is very low. So, it is expected to obtain metallic copper after reaction. Zheng *et al.* [38] and Guo *et al.* [24] have also reported that metallic copper forms during solvothermal synthesis of copper ferrite. Formation of copper oxide has also been reported by Muthukumar *et al.* [36].

For the UAS30 sample, no peaks corresponding to sodium chloride are observed and the peak intensity of metallic copper has increased relative to the ST sample. It can be stated that ultrasonic waves provide higher crystallinity in the synthesized sample. For the UAS60 sample, sodium chloride peaks are appeared again and metallic copper peaks are completely vanished. Broader peaks are also observed so that the peaks corresponding to copper oxide and copper ferrite have overlapped. This can be attributed to the effect of ultrasonication on grain refining.

FTIR spectra for ST, UAS30 and UAS60 samples are shown in Fig. 3b. Peaks at 1588 and 1072 cm^{-1} correspond to C-O stretching bonds. Peaks at 1375 cm^{-1} and 855 cm^{-1} arise from CH_2 and =CH bonds, respectively. All the bonds result from the presence of ethylene glycol on the surface of the synthesized powder [48]. Peaks observed at 545 and 435 cm^{-1} are attributed to oxygen-metal bonds in tetrahedral and octahedral spaces [49]. These characteristic peaks are in accordance with cubic spinel structure illustrated in XRD patterns. Since tetrahedral bonds have higher bonding length than octahedral bonds [50], the vibration frequency of oxygen-metal bonds in tetrahedral spaces is higher than that in octahedral spaces. So, the peak at 435 cm^{-1} is related to oxygen-metal bonds in octahedral spaces and the peak at 545 cm^{-1} relates to oxygen-metal bonds in tetrahedral spaces. This confirms the formation of spinel structure in the synthesized samples.

Microstructure

FESEM micrographs at different magnifications for ST, UAS30 and UAS60 samples are shown in Fig. 4a,b,4c,d and 4e,f, respectively. The microstructure of all the synthesized powders under different conditions contains well-dispersed sub-

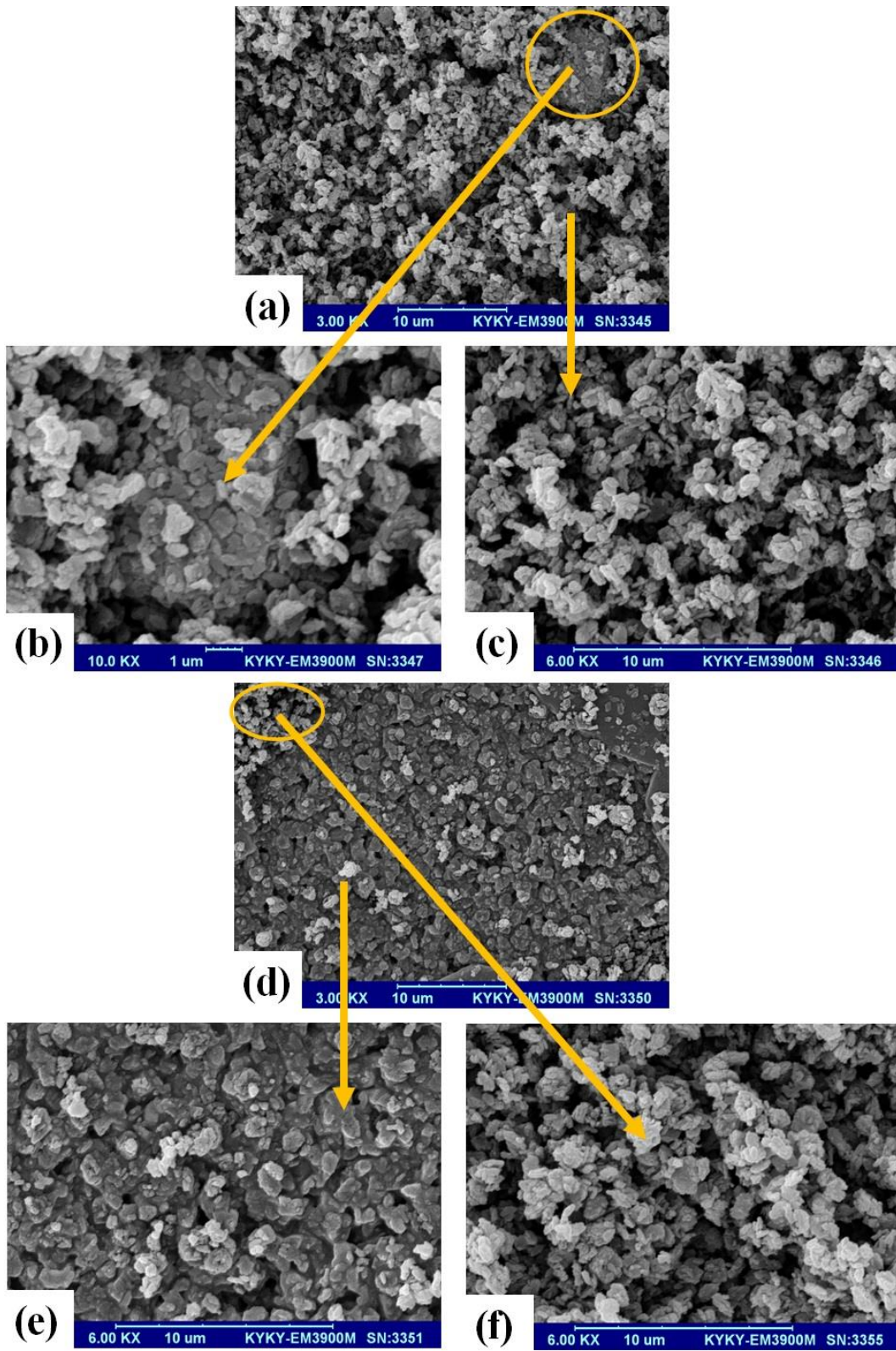


Fig. 2. SEM images at different magnifications for (a-c) U₃O₈ and (d-f) U₆O₁₃ samples.

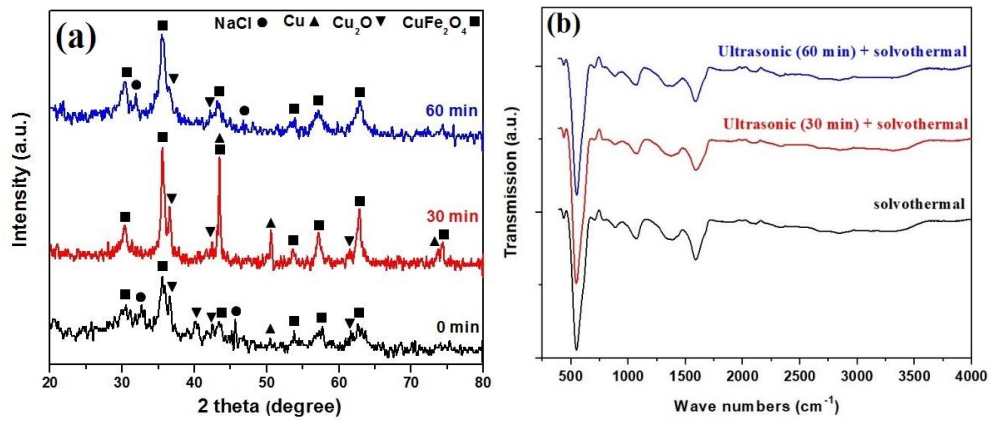


Fig. 3. (a) XRD patterns and (b) FTIR spectra for ST, UAS30 and UAS60 samples.

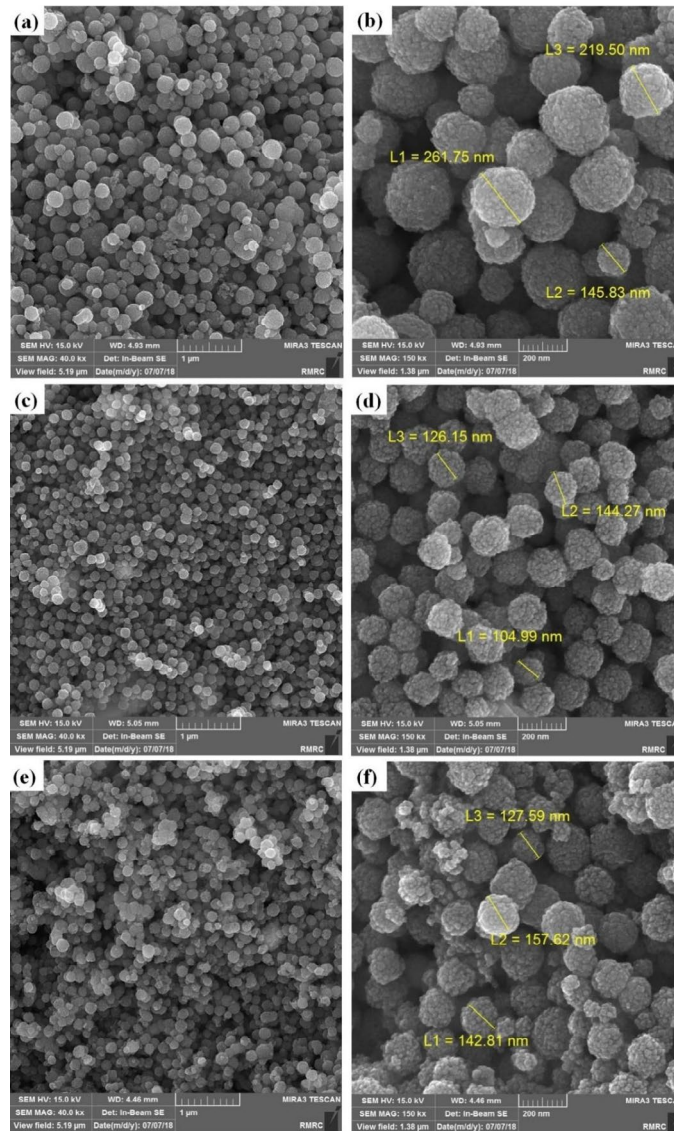


Fig. 4. FESEM micrographs of (a, b) ST, (c, d) UAS30 and (e, f) UAS60 samples.

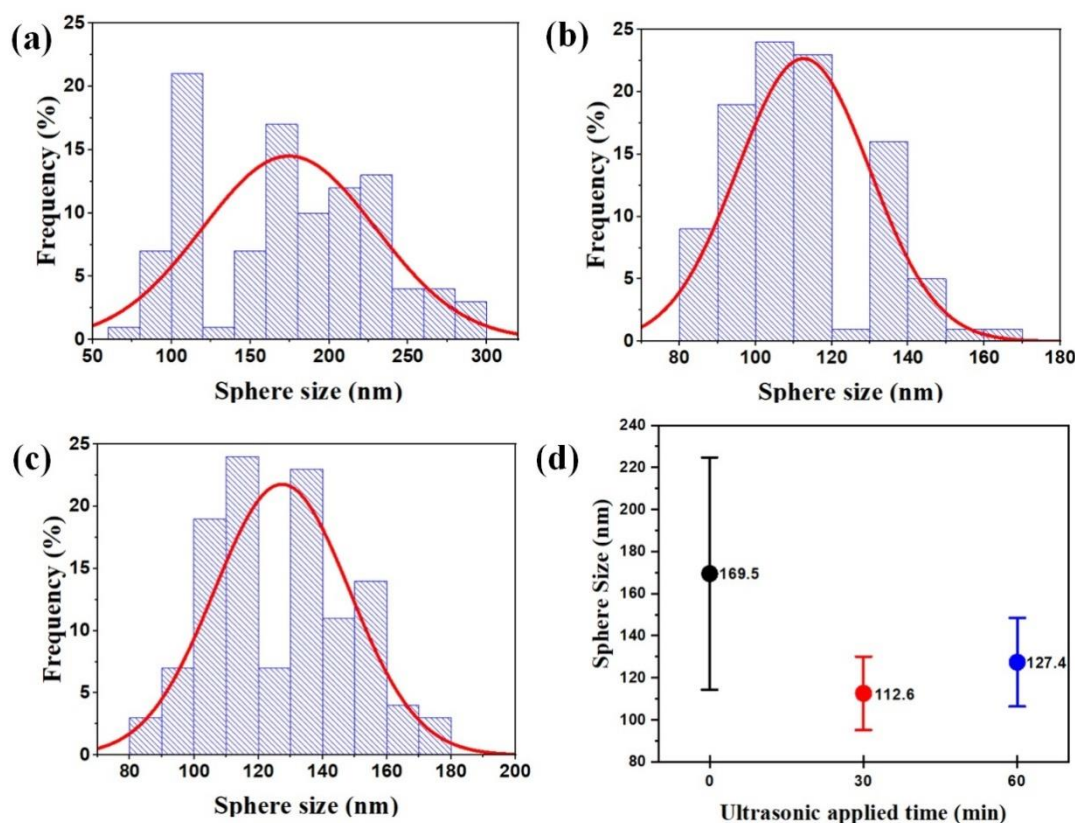


Fig. 5. Size distribution curves of the submicron spheres in (a) ST, (b) UAS30 and (c) UAS60 samples, (d) mean particle size and standard deviation calculated using curves a-c.

micrometer spherical particles with no evidence of agglomeration. Each submicron sphere itself consisted of well-arranged nanoparticles. Since no template has been used in the present work, it can be claimed that nanoparticles have self-assembled during the synthesis process. So, ultrasonic waves can affect the shape, distribution and size of the submicron spheres in the powder. Ultrasonication for 30 min reduces the relative size of the submicron spheres. Increasing the ultrasonication time to 60 min has led to somewhat disordered assembly of the spheres.

Size distribution curves for the submicron spheres are shown in Fig. 5a-c. The mean particle size and the standard deviation of the submicron spheres are calculated and represented in Fig. 5d. The mean particle size of the nanoparticles in the ST, UAS30 and UAS60 samples is 12.4, 11.5 and 12.5 nm, respectively. The results are almost equal to the crystallite sizes calculated according to Scherer equation. This demonstrates that the nanoparticles forming the submicron spheres are

single crystal.

The mean size of the submicron spheres in the ST sample (169.5 nm which is in accordance with 170 nm reported by Zheng *et al.* [38]) is significantly different from that obtained in UAS30 and UAS60 samples (Fig. 5d). 30 min ultrasonication has resulted in finer spheres of about 112.6 nm size. Increasing the ultrasonication time from 30 to 60 min had no significant effect on the size of submicron spheres. On the other hand, it can be seen that the standard deviation for the ST sample is much higher than that obtained for UAS30 and UAS60 samples. As a result, ultrasonication not only reduces the size of submicron spheres but also provides more uniform particle size distribution. But, as was mentioned before, increasing the ultrasonication time reduces the assembly order of the submicron spheres.

Specific surface area and pore distribution

Nitrogen adsorption/desorption curves for ST, UAS30 and UAS60 samples are shown in

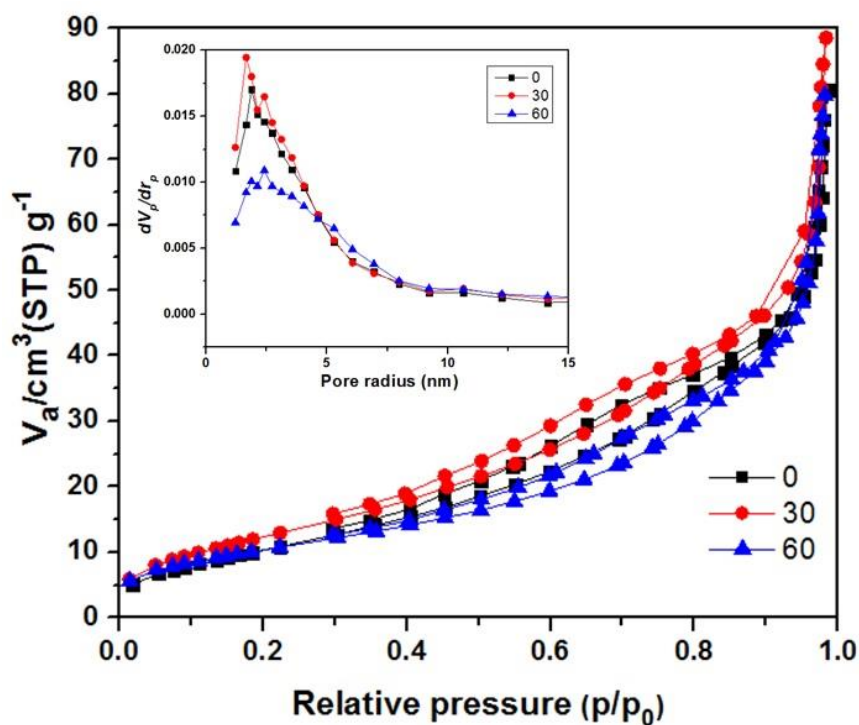


Fig. 6. Nitrogen adsorption/desorption isotherms at 77 K for ST, UAS30 and UAS60 samples.

Table 2. BET specific surface area, total pore volume and mean pore diameter for ST, UAS30 and UAS60 samples.

sample	specific surface area (m^2g^{-1})	total pore volume (cm^3g^{-1})	mean pore diameter (nm)
ST	42.207	0.1245	11.799
UAS30	49.279	0.1370	11.118
UAS60	32.320	0.1234	13.299

Fig. 6. Specific surface area, total pore volume and mean pore diameter are calculated from nitrogen adsorption isotherm obtained via BET method (Table 2). The results show that 30 min ultrasonication has increased the specific surface area. By increasing the ultrasonication time to 60 min, however, the specific surface area has significantly decreased. Total pore volume values show that the UAS30 sample has the highest pore volume, and so, the highest specific surface area. Comparing the ST sample with UAS60 reveals that the pore volume has not markedly changed, but their specific surface area is significantly different. The reason can be explained by comparing their mean pore diameter. According to Table 2, the mean pore diameter in the ST sample is smaller than that in the UAS60 sample. Since smaller pores

have higher surface to volume ratio, the ST sample possesses higher specific surface area. In addition, 30 min ultrasonication has increased the amount of small pores, which means higher specific surface area. However, increasing the ultrasonication time from 30 to 60 min has resulted in fewer but larger pores in the microspheres. To make sure about the results, the inset in Fig. 6 shows the pores' frequency distribution curves calculated using nitrogen adsorption isotherm curve obtained via BJH method. The curves show that the amount of pores larger than 5nm is nearly equal in all three samples, but the amount of pores smaller than 5nm in the UAS60 sample is significantly less than that in ST and UAS30 samples. The frequency distribution peaks for the ST, UAS30 and UAS60 samples are located at pore radius of 1.88, 1.66

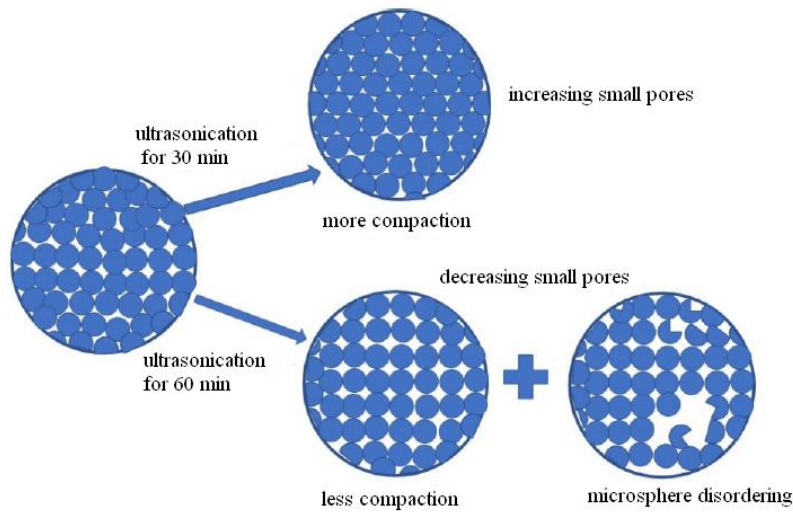


Fig. 7. Schematic representation of the effect of ultrasonic waves on the particle size distribution and the pore size in the microspheres.

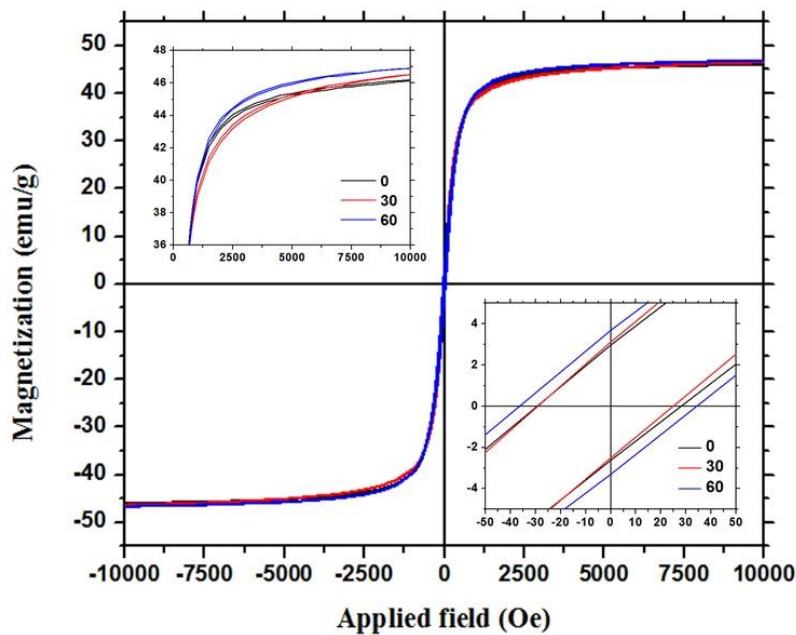


Fig. 8. Magnetization curves versus applied magnetic field for ST, UAS30 and UAS60 samples.

and 2.41 nm, respectively. The minimum pore size belongs to the UAS30 sample, which confirms its higher specific surface area compared with the ST and UAS60 samples. Microstructural images in Fig. 4 also confirm the above findings. On one hand, ultrasonication reduced the total pore volume due to the decreased assembly of the nanoparticles. On the other hand, their disordered assembly provides larger pores, as shown schematically in Fig. 7.

Magnetic properties

Magnetization curves versus applied field are shown in Fig. 8 for ST, UAS30 and UAS60 samples. The insets in Fig. 8 show more details on the differences in magnetization saturation and coercivity of the samples. The relatively steep slope of the magnetization curves implies high permeability and desirable response to the magnetic field. Saturation magnetization,

Table 3. Magnetic properties of CuFe₂O₄ nanostructures in ST, UAS30 and UAS60 samples.

sample	saturation magnetization (emu/g)	remanent magnetization (emu/g)	coercivity (Oe)	squareness ratio
ST	46.19	2.96	28.71	0.064
UAS30	46.51	3.11	27.02	0.066
UAS60	46.89	3.68	35.32	0.078

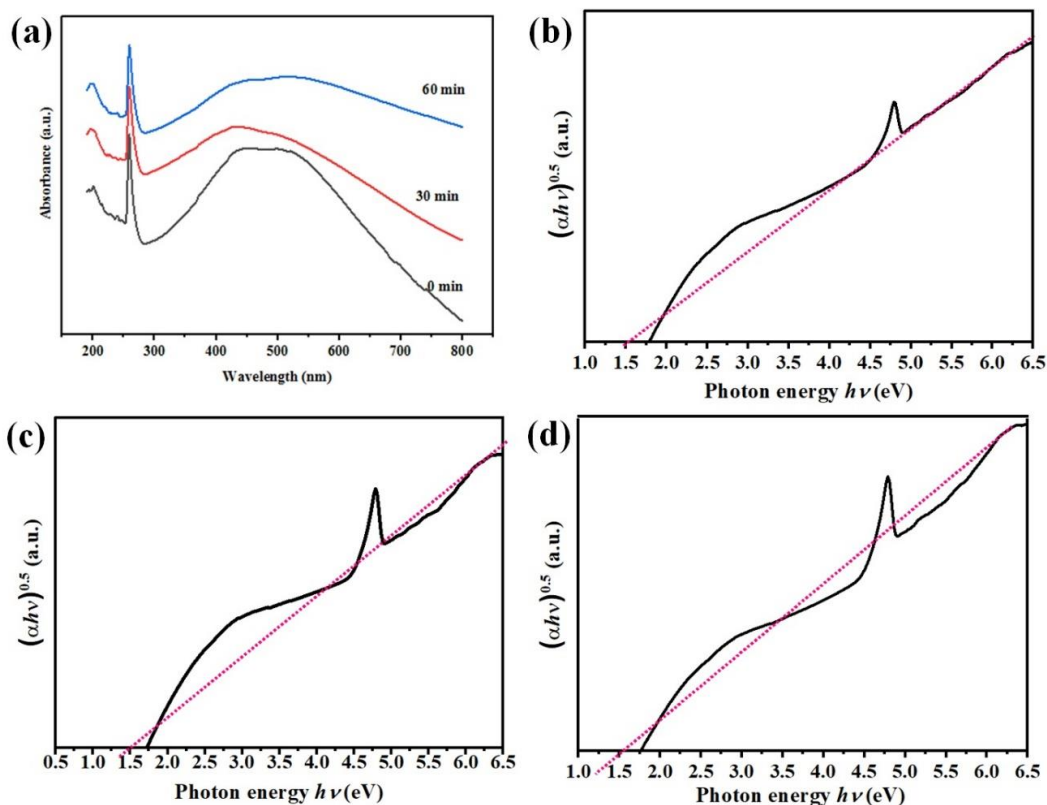


Fig. 9. (a) UV-Vis curves for ST, UAS30 and UAS60 samples, (b-d) estimated band gap energy.

remanent magnetization and coercivity values as well as the squareness ratio (the ratio of remanent to saturation magnetization) of the samples are listed in Table 3. As can be seen, lack of hysteresis loop, low coercivity, negligible squareness ratio, and high saturation magnetization imply that the synthesized powders have superparamagnetic behavior.

There is little difference in saturation magnetization values of samples (less than 1 emu/g). So, it can be concluded that ultrasonic waves had no effect on the magnetization. Also, there is no significant difference in coercivity of the ST and UAS30 samples. Increasing the ultrasonication time from 30 to 60 min, however, slightly increases the coercivity. It has proved that

in the superparamagnetic materials, coercivity increases with particle size. But, as was mentioned before, the particle size of all the synthesized powders are nearly the same. So, this theory cannot be valid for the present work. Guo *et al.* [51] reported that the nanoparticles assembly may affect the magnetic properties. As mentioned above, ultrasonication for 60min reduces the order of the nanoparticles assembly. So, the disruption of the nanoparticles assembly may be the reason for the higher coercivity of the UAS60 sample.

Optical properties

Fig. 9a shows optical adsorption of ST, UAS30 and UAS60 samples. All the samples have adsorption in the visible range (400-700 nm) and

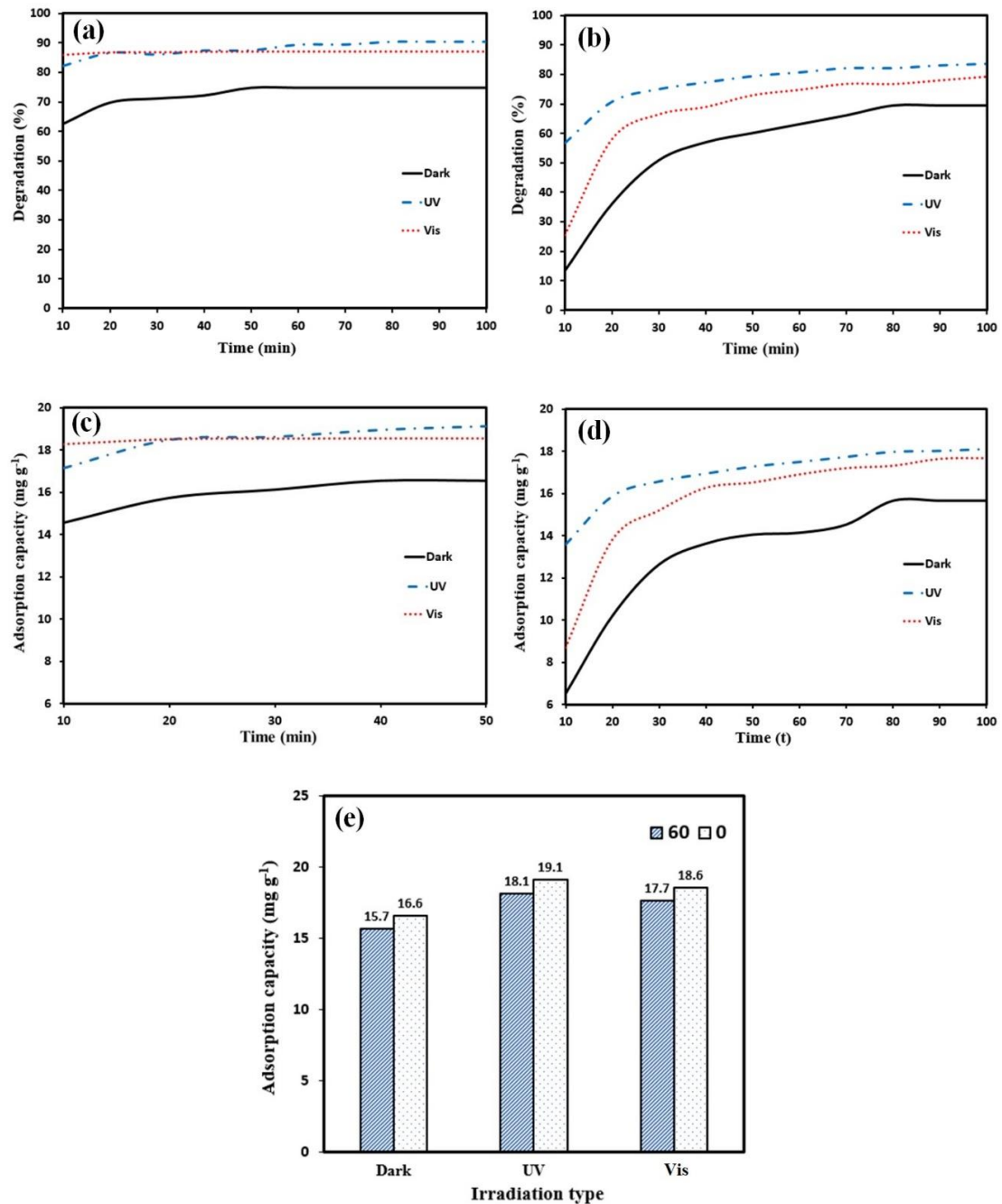


Fig. 10. (a,b) Dye degradation, (c,d,e) adsorption capacity of the ST and UAS60 powders under UV light, visible light and in darkness.

the most adsorption occurs in the range of 425–525 nm. For all the samples, the band gap energy calculated based on the Tauc relation (Fig. 9b,c,d) was about 1.5 eV which is consistent with the reported values by other researchers for copper ferrite powders synthesized via solvothermal method, i.e. 1.69 eV reported by Shen *et al.* [40] and 1.32 eV reported by Atacan *et al.* [32].

Photocatalytic properties

Methyl orange degradation curves versus time under different light exposure conditions (i.e. darkness, visible light and 254 nm UV light) are shown in Figs. 10a and 10b for ST and UAS60 samples. For both samples, dye removal in darkness has enhanced by increasing the time from 10 to 100 min. The highest degradation rate

is observed in the initial stages of dye removal. The adsorption rate for the ST sample decreases after 20 min, while this decrement occurs after 30 min for the UAS60 sample. The probability of the interaction between the adsorbent and the adsorbate increases by the number of adsorption sites. So, the most adsorption occurs at the initial stages. By occupying the sites on the surface of the adsorbent, adsorption rate decreases until it reaches a constant value.

It can be seen from Figs. 10a and 10b that color degradation under visible or UV exposure has significantly increased compared to dye removal in darkness. This is indicative of photocatalytic nature in addition to surface adsorption properties. For the ST sample, there is no significant difference between degradation under visible or UV light. For the UAS60 sample, however, more degradation occurs under UV light, particularly at initial times. It should be noted again that for the ST sample, surface adsorption and optical interactions have mostly occurred during the first minute. This implies the high performance of the catalyst which is of high importance for industrial applications. Nagalakshmi *et al.* [10] have reported the dye removal efficiency of about 85% using TiO₂ photocatalyst after 200 min, while Zamani *et al.* [17] have reported the dye removal efficiency of about 85% after 30 min by using ZnFe₂O₄@MnO magnetic nanocomposite. In the present work, the same efficiency is obtained by the CuFe₂O₄ photocatalyst in just 10 min.

Dye removal capacity curves under different light exposure conditions (i.e. darkness, visible light and 254 nm UV light) for ST and UAS60 samples are shown in Figs. 10c and 10d. For better comparison, the maximum adsorption capacity is also extracted from each curve and shown as a histogram in Fig. 10e. According to Fig. 10c, the adsorption capacity under UV light, visible light and in darkness for the ST sample are 19.12, 18.57 and 16.54 mg g⁻¹, respectively, while these values for the UAS60 sample reach 18.13, 17.66 and 15.65 mg g⁻¹, respectively (Fig. 10d). As mentioned in section 3.2.3, the ST sample has higher specific surface area. So, it has higher adsorption capacity. It adsorbs 16.6 mg per 1 g of the adsorbent in darkness due to the physical adsorption on the surface of the nanoparticles. The adsorption capacity increases to 19.1 mg g⁻¹ under UV light. This increase (about 2.5 mg g⁻¹) may be due to the photocatalytic activity of the synthesized nano-ferrites.

CONCLUSIONS

The aim of the present work was to synthesize self-assembled copper ferrite nanoparticles using ultrasonic-assisted solvothermal method. The conclusions can be summarized as follows:

- 1- Although ultrasonication cannot directly lead to the formation of copper ferrite, it significantly affected the properties of the synthesized powders.
- 2- Copper ferrite nanoparticles containing self-assembled submicron spheres were synthesized successfully. The nanoparticles had superparamagnetic behavior with specific surface area of about 42 m²g⁻¹. Saturation magnetization of about 46 emu/g, allows their easy separation from the medium. They also had high catalytic rate (less than 10 min).
- 3- Finer copper ferrite microspheres with more uniform size distribution were obtained via ultrasonication. Ultrasonication for 30 min increased the specific surface area of the nanoparticles, but further ultrasonication had reverse effect and decreased their specific surface area.
- 4- The obtained results showed that the synthesized nanoparticles are good candidates for magnetic and photocatalytic applications and they are also able to degrade azo dyes (like methyl orange) under both visible and UV radiations.

CONFLICT OF INTEREST

The authors declare that they have no competing interests.

REFERENCES

- [1] Holkar C. R., Jadhav A. J., Pinjari D. V., Mahamuni N. M., Pandit A. B., (2016), A critical review on textile wastewater treatments: Possible approaches. *J. Environ. Manage.* 182: 351-366.
- [2] Raval N. P., Shah P. U., Shah N. K., (2016), Adsorptive amputation of hazardous azo dye Congo red from wastewater: A critical review. *Environ. Sci. Pollut. Res.* 23: 14810-14853.
- [3] Tadjarodi A., Imani M., (2016), Synthesis of porous CdO sheet-like nanostructure based on soft template model and its application in dye pollutants adsorption. *Int. J. Nano Dimens.* 7: 150-159.
- [4] Hosseini S. A., Davodian M., Abbasian A. R., (2017), Remediation of phenol and phenolic derivatives by catalytic wet peroxide oxidation over Co-Ni layered double nano hydroxides. *J. Taiwan. Inst. Chem. E.* 75: 97-104.
- [5] Chekir N., Benhabiles O., Tassalit D., Laoufi N. A., Bentahar F., (2016), Photocatalytic degradation of methylene blue in aqueous suspensions using TiO₂ and ZnO. *Desalin. Water*

- Treat.* 57: 6141-6147.
- [6] Li S., Chen J., Liu Y., Xu K., Liu J., (2019), In situ anion exchange strategy to construct flower-like BiOCl/BiOCCOOH p-n heterojunctions for efficiently photocatalytic removal of aqueous toxic pollutants under solar irradiation. *J. Alloys Compd.* 781: 582-588.
- [7] Li S., Chen J., Jiang W., Liu Y., Ge Y., Liu J., (2019), Facile construction of flower-like bismuth oxybromide/bismuth oxide formate p-n heterojunctions with significantly enhanced photocatalytic performance under visible light. *J. Colloid Interface Sci.* 548: 12-19.
- [8] Bhatkhande D. S., Pangarkar V. G., Beenackers A. A. C. M., (2002), Photocatalytic degradation for environmental applications – A review. *J. Chem. Technol. Biotechnol.* 77: 102-116.
- [9] Zakeri S. M. E., Asghari M., Feilizadeh M., Vosoughi M., (2014), A visible light driven doped TiO₂ nanophotocatalyst: Preparation and characterization. *Int. J. Nano Dimens.* 5: 329-335.
- [10] Nagalakshmi M., Karthikeyan C., Anusuya N., Brundha C., Basu M. J., Karuppuachamy S., (2017), Synthesis of TiO₂ nanofiber for photocatalytic and antibacterial applications. *J. Mater. Sci.: Mater. Elect.* 28: 15915-15920.
- [11] Abbasian A. R., Omidvar-Askary N., (2019), Microstructural and mechanical investigation of high alumina refractory castables containing nano-titania. *Ceram. Int.* 45: 287-298.
- [12] Karthikeyan C., Thamima M., Karuppuachamy S., (2019), Dye removal efficiency of perovskite structured CaTiO₃ nanospheres prepared by microwave assisted method. *Mater. Today: Proceedings.* In Press.
- [13] Tong H., Ouyang S., Bi Y., Umezawa N., Oshikiri M., Ye J., (2012), Nano-photocatalytic Materials: Possibilities and Challenges. *Adv. Mater.* 24: 229-251.
- [14] Khaksar E., Shafiee Afarani M., Samimi A., (2014), In situ solvothermal crystallization of TiO₂ nanostructure on Alumina Granules for photocatalytic wastewater treatment. *J. Mater. Eng. Perform.* 23: 92-100.
- [15] Gómez-Pastora J., Dominguez S., Bringas E., Rivero M. J., Ortiz I., Dionysiou D. D., (2017), Review and perspectives on the use of magnetic nanophotocatalysts (MNPCs) in water treatment. *Chem. Eng. J.* 310: 407-427.
- [16] Kefeni K. K., Mamba B. B., Msagati T. A. M., (2017), Application of spinel ferrite nanoparticles in water and wastewater treatment: A review. *Sep. Purif. Technol.* 188: 399-422.
- [17] Zamani A., Seyed Sadjadi M., Mahjoub A. R., Yousefi M., Farhadyar N., (2020), Synthesis and characterization ZnFe₂O₄@MnO and MnFe₂O₄@ZnO magnetic nanocomposites: Investigation of photocatalytic activity for the degradation of Congo Red under visible light irradiation. *Int. J. Nano Dimens.* 11: 58-73.
- [18] Mohamed R. M., McKinney D. L., Sigmund W. M., (2012), Enhanced nanocatalysts. *Mater. Sci. Eng. R.* 73: 1-13.
- [19] Wang T., Zhang L., Wang H., Yang W., Fu Y., Zhou W., Yu W., Xiang K., Su Z., Dai S., Chai L., (2013), Controllable synthesis of hierarchical porous Fe₃O₄ particles mediated by Poly(diallyldimethylammonium chloride) and their application in arsenic removal. *ACS Appl. Mater. Interfaces.* 5: 12449-12459.
- [20] Sapna Budhiraja N., Kumar V., Singh S. K., (2019), Shape-controlled synthesis of superparamagnetic ZnFe₂O₄ hierarchical structures and their comparative structural, optical and magnetic properties. *Ceram. Int.* 45: 1067-1076.
- [21] Guo P., Lv M., Han G., Wen C., Wang Q., Li H., Zhao X., (2016), Solvothermal synthesis of hierarchical colloidal nanocrystal assemblies of ZnFe₂O₄ and their application in water treatment. *Materials (Basel).* 9: 806.
- [22] Jing P., Du J., Wang J., Lan W., Pan L., Li J., Wei J., Cao D., Zhang X., Zhao C., (2015), Hierarchical SrTiO₃/NiFe₂O₄ composite nanostructures with excellent light response and magnetic performance synthesized toward enhanced photocatalytic activity. *Nanoscale.* 7: 14738-14746.
- [23] Zhu M., Meng D., Wang C., Diao G., (2013), Facile fabrication of hierarchically porous CuFe₂O₄ nanospheres with enhanced capacitance property. *ACS Appl. Mater. Interfaces.* 5: 6030-6037.
- [24] Guo X., Wang K., Li D., Qin J., (2017), Heterogeneous photo-fenton processes using graphite carbon coating hollow CuFe₂O₄ spheres for the degradation of methylene blue. *Appl. Surf. Sci.* 420: 792-801.
- [25] Sun Z., Liu L., Zeng Jia D., Pan W., (2007), Simple synthesis of CuFe₂O₄ nanoparticles as gas-sensing materials. *Sens. Actuators B.* 125: 144-148.
- [26] Kombaiah K., Vijaya J. J., Kennedy L. J., Bououdina M., Al-Najar B., (2018), Conventional and microwave combustion synthesis of optomagnetic CuFe₂O₄ nanoparticles for hyperthermia studies. *J. Phys. Chem. Solids.* 115: 162-171.
- [27] Hou H., Xu G., Tan S., Zhu Y., (2017), A facile sol-gel strategy for the scalable synthesis of CuFe₂O₄ nanoparticles with enhanced infrared radiation property: influence of the synthesis conditions. *Infrared Phys. Technol.* 85: 261-265.
- [28] Agouriane E., Rabi B., Essoumhi A., Razouk A., Sahlaoui M., Costa B., Sajjeddine M., (2016), Structural and magnetic properties of CuFe₂O₄ ferrite nanoparticles synthesized by co-precipitation. *J. Mater. Environ. Sci.* 7: 4116-4120.
- [29] Zhang E., Wang L., Zhang B., Xie Y., Wang G., (2019), Shape-controlled hydrothermal synthesis of CuFe₂O₄ nanocrystals for enhancing photocatalytic and photoelectrochemical performance. *Mater. Chem. Phys.* 235: 121633-121638.
- [30] Yang X., Zhang S., Yu Q., Sun P., Liu F., Lu H., Yan X., Zhou X., Liang X., Gao Y., (2018), Solvothermal synthesis of porous CuFe₂O₄ nanospheres for high performance acetone sensor. *Sens. Actuators. B.* 270: 538-544.
- [31] Shaterian M., Rezvani A., Abbasian A. R., (2020), Controlled synthesis and self-assembly of ZnFe₂O₄ nanoparticles into microspheres by solvothermal method. *Mater. Res. Express.* 6: 1250-1255.
- [32] Atacan K., Topaloğlu B., Özacar M., (2018), New CuFe₂O₄/amorphous manganese oxide nanocomposites used as photocatalysts in photoelectrochemical water splitting. *Appl. Catal. A.* 564: 33-42.
- [33] Hou H., Xu G., Tan S., Xiang S., (2018), Effects of solvents on the synthesis and infrared radiation emissivity of CuFe₂O₄ spinels. *J. Alloys Compd.* 763: 736-741.
- [34] Kurian J., Mathew M. J., (2018), Structural, optical and magnetic studies of CuFe₂O₄, MgFe₂O₄ and ZnFe₂O₄ nanoparticles prepared by hydrothermal/solvothermal method. *J. Magn. Magn. Mater.* 451: 121-130.
- [35] Liu X., Qi X., Zhang L., (2018), 3D hierarchical magnetic hollow sphere-like CuFe₂O₄ combined with HPLC for the simultaneous determination of Sudan I-IV dyes in preserved bean curd. *Food Chem.* 241: 268-274.
- [36] Muthukumar K., Lakshmi D. S., Acharya S. D., Natarajan S., Mukherjee A., Bajaj H., (2018), Solvothermal synthesis of magnetic copper ferrite nano sheet and its antimicrobial studies. *Mater. Chem. Phys.* 209: 172-179.

- [37] Phuruangrat A., Kuntalue B., Dumrongrojthanath P., Thongtem T., Thongtem S., (2018), Microwave-assisted solvothermal synthesis of cubic ferrite (MFe_2O_4 , M= Mn, Zn, Cu and Ni) nanocrystals and their magnetic properties. *Dig. J. Nanomater. Biostruct.* 13: 563-568.
- [38] Zheng J., Lin Z., Liu W., Wang L., Zhao S., Yang H., Zhang L., (2014), One-pot synthesis of $CuFe_2O_4$ magnetic nanocrystal clusters for highly specific separation of histidine-rich proteins. *J. Mater. Chem. B.* 2: 6207-6214.
- [39] Chatterjee B. K., Bhattacharjee K., Dey A., Ghosh C. K., Chattopadhyay K. K., (2014), Influence of spherical assembly of copper ferrite nanoparticles on magnetic properties: Orientation of magnetic easy axis. *Dalton Trans.* 43: 7930-7944.
- [40] Shen Y., Wu Y., Xu H., Fu J., Li X., Zhao Q., Hou Y., (2013), Facile preparation of sphere-like copper ferrite nanostructures and their enhanced visible-light-induced photocatalytic conversion of benzene. *Mater. Res. Bull.* 48: 4216-4222.
- [41] Kafi-Ahmadi L., Mohammadzadeh-Hesar R., Khademinia S., (2018), Influence of reaction parameters on crystal phase growth and optical properties of ultrasonic assisted hydro- and solvothermal synthesized sub-micrometer-sized CdS spheres. *Int. J. Nano Dimens.* 9: 346-356.
- [42] Hosseini S. A., Majidi V., Abbasian A. R., (2018), Photocatalytic desulfurization of dibenzothiophene by $NiCo_2O_4$ nanospinel obtained by an oxidative precipitation process modeling and optimization. *J. Sulfur Chem.* 39: 119-129.
- [43] Mills G., Li Z., Meisel D., (1988), Zero-dimensional excitons in semiconductor clusters. *J. Phys. Chem.* 92: 822-830.
- [44] Tauc J., Mentel A., (1972), States in the gap. *J. Non-Cryst. Solids.* 8: 569-585.
- [45] Tran P. H., Thi Hang A.-H., (2018), Deep eutectic solvent-catalyzed arylation of benzoxazoles with aromatic aldehydes. *RSC Adv.* 8: 11127-11133.
- [46] Zaharescu M., Mocioiu O. C., (2013), Infrared Spectroscopy, in: T. Schneller, R. Waser, M. Kosec, D. Payne (Eds.) *Chem. Solut. Depos. Func. Oxide Thin Films*, Springer Vienna, Vienna, 213-230.
- [47] Nakamoto K. (2009). *Infrared and Raman Spectra of Inorganic and Coordination Compounds: Part B: Applications in Coordination, Organometallic, and Bioinorganic Chemistry*, Sixth Edition ed., John Wiley & Sons, Hoboken, New Jersey.
- [48] Guo P., Zhang G., Yu J., Li H., Zhao X. S., (2012), Controlled synthesis, magnetic and photocatalytic properties of hollow spheres and colloidal nanocrystal clusters of manganese ferrite. *Colloids Surf. A.* 395: 168-174.
- [49] Hosseini S. A., Abbasian A. R., Gholipour O., Ranjan S., Dasgupta N., (2019), Adsorptive removal of arsenic from real sample of polluted water using magnetic GO/ $ZnFe_2O_4$ nanocomposite and $ZnFe_2O_4$ nanospinel. *Int. J. Environ. Sci. Technol.* 16: 7455-7466.
- [50] Abbasian A. -R., Shafiee Afarani M., (2019), One-step solution combustion synthesis and characterization of $ZnFe_2O_4$ and $ZnFe_{1.6}O_4$ nanoparticles. *Appl. Phys. A.* 125: 721-726.
- [51] Guo P., Wang R., Xue J., Xu B., Sang Y., Li H., Zhao X. S., (2017), Assembly of colloidal cuprous oxide nanocrystals and study of its magnetic and electrocatalytic properties. *Colloids Surf. A.* 522: 295-303.